

Calibration and preparation of field measurements of oblique wave run-up and overtopping on dikes using laser scanners

Patrick Oosterlo^{a,*}, Bas Hofland^a, Jentsje W. van der Meer^{a,b,c}, Maarten Overduin^d,
Gosse Jan Steendam^d

^a Delft University of Technology, P.O. Box 5048, 2600 GA, Delft, the Netherlands

^b Van der Meer Consulting BV, Akkrum, the Netherlands

^c IHE Delft, Delft, the Netherlands

^d Infram Hydren, Maarn, the Netherlands

ARTICLE INFO

Keywords:

LIDAR
Laser scanner
Wave run-up
Wave overtopping
Dike
Numerical wave modelling

ABSTRACT

Wave overtopping is typically measured in the field using overtopping tanks. In this paper, an alternative system is developed that uses two laser scanners. The system also measures wave run-up, as well as run-up depths and velocities, both during perpendicular and oblique waves on a dike in the field. The paper considers the first calibration tests with the system in the field, with perpendicular and oblique waves generated by the wave run-up simulator on a grass dike slope. Furthermore, simulations are performed with the numerical wave model SWASH, to gain more insight in the potential performance of the system during actual oblique wave attack during a storm. The run-up is determined from the measured elevation and reflection intensity, which agrees well with the visually observed run-up. Run-up depths and front velocities can be determined accurately as well. The (virtual) wave overtopping discharge can be calculated from the data, which agrees well with the most commonly used overtopping equations for perpendicularly incident waves. Finally, from the simulated run-up data of obliquely incident waves, it is concluded that an estimate can be obtained of the incident wave period and wave angle of incidence at the toe of the structure.

1. Introduction

In the past, the required crest height of dikes was determined by assessing the wave run-up height. Wave run-up heights and run-up depths (layer thicknesses, flow depths) and velocities were measured in the lab and field often in the past, but the latter measurements are difficult because of turbulence and aeration (Schüttrumpf and Van Gent, 2004; Van der Meer et al., 2010). The measurements are performed often using resistance type gauges, which require a certain minimum run-up depth, or step gauges, which have a coarse resolution. Other techniques that have been used are e.g. stereo-photogrammetry (e.g. De Vries et al., 2011) and ultrasonic altimeters (e.g. Matias et al., 2014). Nowadays, dikes are usually designed using the mean wave overtopping discharge. Typically, wave overtopping is measured in the field using wave overtopping tanks (e.g. De Rouck et al., 2009; Van der Meer et al., 2019; Wenneker et al., 2016), but overtopping measurements in the field are scarce. Overtopping tanks are a robust method to measure wave

overtopping, but fixed at a certain location and at a fixed elevation.

An alternative and more flexible solution was developed in Oosterlo et al. (2019) based on Hofland et al. (2015), using two terrestrial laser scanners or LIDARs. Laser scanners are used often for terrestrial measurements, either from a plane (see Guenther et al., 2000; Vosselman and Maas, 2010) or (autonomous) car (e.g. Spore et al., 2014; Wübbold et al., 2012). More recently, they were applied in coastal engineering applications, to measure morphological changes caused by waves (Almeida et al., 2015; Vousdoulas et al., 2014) and the water surface or waves in the field (Blenkinsopp et al., 2010; Maslov et al., 2000) or in a flume (Allis et al., 2011; Blenkinsopp et al., 2012; Streicher et al., 2013). Several studies have also used laser scanners to measure wave run-up, in the field (e.g. Brodie et al., 2012) or in a flume (Hofland et al., 2015; Vousdoulas et al., 2014). However, the studies that measured wave run-up in the field generally used a lower scan frequency, thus not obtaining the instantaneous water surface and not being able to measure the wave run-up with a high temporal resolution.

* Corresponding author.

E-mail addresses: P.Oosterlo@tudelft.nl (P. Oosterlo), B.Hofland@tudelft.nl (B. Hofland), jm@vandermeerconsulting.nl (J.W. van der Meer), maarten.overduin@infram-hydren.nl (M. Overduin), gosse.jan.steendam@infram-hydren.nl (G.J. Steendam).

<https://doi.org/10.1016/j.coastaleng.2021.103915>

Received 31 July 2020; Received in revised form 25 March 2021; Accepted 1 May 2021

Available online 12 May 2021

0378-3839/© 2021 The Author(s). Published by Elsevier B.V. This is an open access article under the CC BY license (<http://creativecommons.org/licenses/by/4.0/>).

The system as developed in Oosterlo et al. (2019) can measure the wave run-up, front velocities and run-up depths of up-rushing waves on a dike in field situations. The virtual wave overtopping can be calculated at any elevation from these measurements as well. The present paper summarises the work of Oosterlo et al. (2019) and extends it with an analysis of oblique wave attack, with field tests with the wave run-up simulator, and with simulations with the phase-resolving numerical wave model SWASH, Simulating WAVes till SHore (Zijlema et al., 2011).

The goal of this paper is to gain full insight in the capabilities of the laser scanners in measuring both perpendicular and obliquely incident waves. To this end, the present paper describes the analysis and calibration with perpendicular and oblique waves physically simulated with the run-up simulator on an actual grass dike slope, as well as numerical simulations of obliquely incident waves with the SWASH model. This paper compares the data as measured by the laser scanners with data from video recordings, 'surf boards' (floaters), paddle wheels and the SWASH model. Furthermore, the results are compared to the most commonly used wave run-up and overtopping equations (EurOtop, 2018). If this calibration is successful, the laser scanner system will be placed next to two overtopping tanks on a dike in the Eems-Dollard estuary in the north of the Netherlands, to measure the wave run-up and overtopping during actual severe winter storms.

The outline of this paper is as follows. Section 2 describes the approach and set-up of the system, based on Oosterlo et al. (2019). After that, section 3 gives a short summary of the post-processing and data analysis. For the full description, the reader is referred to Oosterlo et al. (2019). The validation of the measured parameters follows in section 4, first for perpendicular wave attack as previously described in Oosterlo et al. (2019). Section 5 presents the results for obliquely incident waves. The section that treats the oblique wave attack not only discusses the field tests, but also gives a description of the numerical analysis of the system for the interaction with an actual oblique wave field. Furthermore, the section discusses the optimisation of the laser scanner system. Finally, section 6 gives the conclusions and presents an outlook on the next steps in this study.

2. Approach and system set-up

The laser scanner system was tested with waves generated by the wave run-up simulator (Van der Meer, 2011) on a dike in Friesland, the Netherlands. The wave run-up simulator is a 7 m-tall vertical tank,

which can be filled with water to a certain level. By quickly opening the bottom of the tank, the tank drains, thereby simulating an individual 'wave' running up the slope. After the tank has drained, the bottom of the tank is closed again, and the tank is filled with water by pumps once more. The time series or steering file of filling levels of the simulator are derived from a Rayleigh distribution with an assumed nearshore significant wave height H_s of 2 m and a peak period T_p of 5.7 s, see also Steendam et al. (2017).

Refer to the left panel of Fig. 2 for the system set-up and instrumentation on the dike slope. The dike slope consists of basalt blocks until 4.16 m + NAP (Normaal Amsterdams Peil, Dutch ordnance level), asphalt until 6.34 m + NAP and grass until the crest at 9.49 m + NAP. The tests were performed on the upper slope consisting of grass, with the mean slope being approximately 1:5. The wave run-up simulator was placed just below the transition from asphalt to grass, at 6 m + NAP. For tests with the simulator, the modelled storm water level is considered to be located at the same location as the outlet of the simulator. Therefore, the origin of the coordinate system was placed at the simulator as well, with x-coordinates being horizontal, z-coordinates being vertical and y-coordinates being in the lengthwise direction of the dike, see the left panel of Figs. 2 and 3. Complicating factors compared to the previous (lab) research on concrete or wooden slopes are the convex dike slope, wave-induced erosion of the grass slope during testing, the blades of grass, which might obfuscate a thin layer of water, as well as water infiltrating into the slope.

The present laser scanner system uses two SICK LMS511pro HR laser scanners, a cheap laser scanner with a near-infrared (905 nm) laser beam, which is the newest version of a commonly used laser scanner in previous research (e.g. in Hofland et al., 2015; Streicher et al., 2013). Fig. 1 shows the calibration set-up at the dike. The system consists of two laser scanners, attached to an easily relocatable pole placed perpendicular to the dike slope. The laser scanners were mounted at heights of 5.17 m and 5.50 m above the slope. The laser scanners measure the distance R to a surface by measuring the time that the reflection of a laser pulse takes to reach the laser again. The reflected signal intensity $RSSI$ (Received Signal Strength Indicator, a dimensionless value between 0 and 255) is measured as well, which provides information on the type of surface. The run-up heights and depths, front velocities, and wave overtopping volumes and discharges can be determined from the R and $RSSI$ data. The scanners have a sampling frequency of 50 Hz and are synchronised. The two laser scanners each scan a line parallel to one

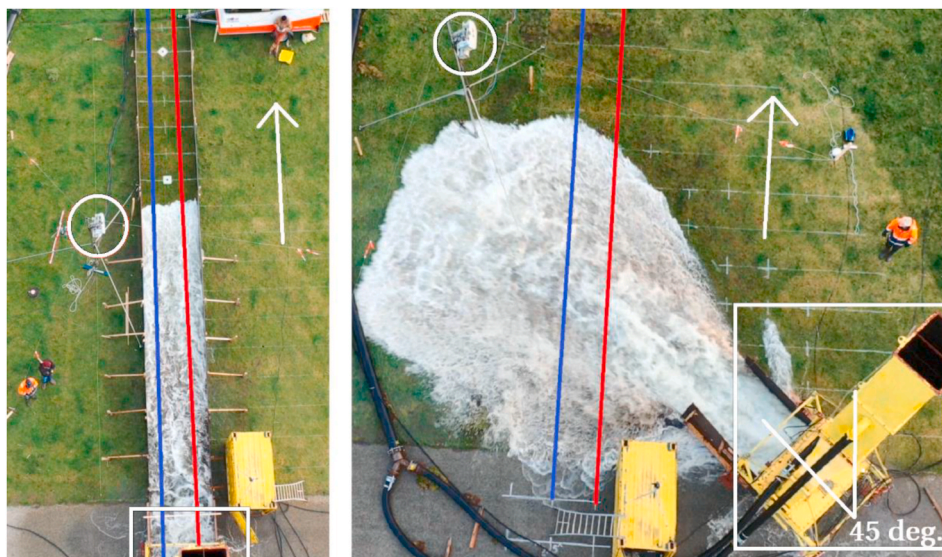


Fig. 1. System overview during perpendicular (left panel) and obliquely (right panel) incident waves. Laser scanners (white circle), run-up simulator (white rectangle), laser scanner scan lines (blue and red lines), up-slope direction (arrows) and 45° angle indicated. (For interpretation of the references to colour in this figure legend, the reader is referred to the Web version of this article.)

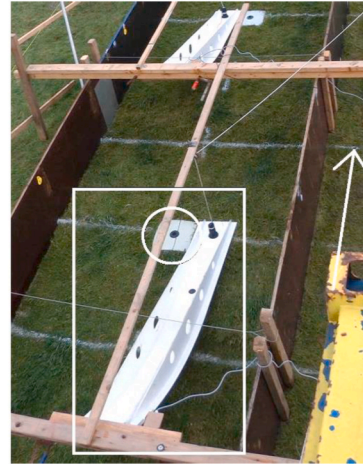
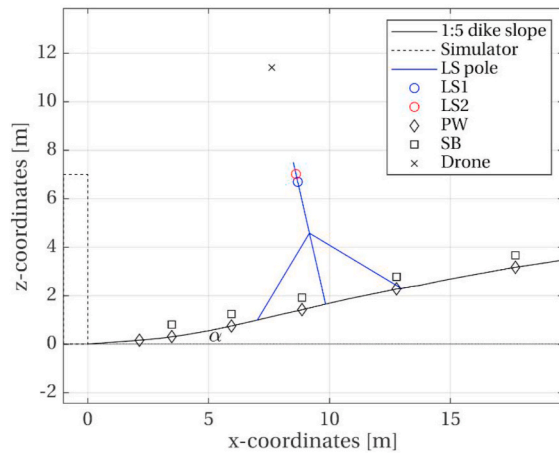


Fig. 2. Left: Side view of system set-up and instrumentation. x-coordinates horizontal, z-coordinates vertical, y-coordinates perpendicular to the figure. α [°] is the slope angle. LS pole is the laser scanner pole, LS1 the lower laser scanner, LS2 the upper laser scanner. PW are the 6 paddle wheels; SB the five surf boards. Right: Example of surf board (white rectangle) and paddle wheel (white circle). Up-slope direction indicated by the arrow.

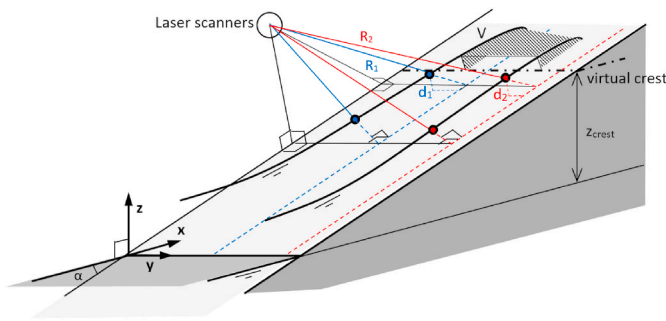


Fig. 3. System set-up as used for the conversion of measured distances (R_1 [m] and R_2 [m], blue and red lines) in polar coordinates to cartesian x,y,z-coordinates [m] according to the coordinate system as shown. Dike slope α [°], laser scan lines (blue and red dashed lines), scanned points on water surface (blue and red dots), virtual crest level z_{crest} [m], run-up depths d_1 [m] and d_2 [m], and virtual overtopping volume V [m³] indicated. (For interpretation of the references to colour in this figure legend, the reader is referred to the Web version of this article.)

another, running from the dike toe to the crest, as indicated by the blue and red lines in Fig. 1. The height of the laser scanners and the distance between both scan lines are adjustable.

The left panel of Fig. 2 shows the locations of all the instruments. For the calibration, the laser data were compared with data obtained by the other instruments. Run-up heights and front velocities were determined from videos recorded by a drone flying above the system. Five ‘surf boards’ measured the run-up depths. The surf boards are curved boards, which are hinged about 1 m above the slope and which float on top of the flowing water. The rotation at the hinge is measured and gives the run-up depth, see e.g. Van der Meer et al. (2010). Six paddle wheels or impellers measured the velocities near the ground. The right panel of Fig. 2 shows two of the surf boards and paddle wheels. Note that the surf boards were mounted only during separate tests where the laser scanners were not used, since they block the view for the laser scanners. An accelerometer was attached to the upper laser scanner, to correlate possible outliers with potentially occurring vibrations. Finally, a relation between the filling level of the simulator and the resulting run-up height was determined from several visually observed run-up heights at this location.

First, tests were performed for perpendicularly incident waves, where for each test seven different known run-up levels (simulator filling levels from 1 m to 7 m) were repeated three times (21 waves in

total) to obtain increased statistical reliability, see also <https://youtu.be/KCfflQ-TPtk>. Filling levels of 1 m–5 m correspond to run-up levels of 0.88 m–3.2 m. Filling levels of 6 m and 7 m overtopped the dike. With these generated run-up levels, the influence of a large range of environmental conditions, e.g. producing artificial wind and rain, and laser scanner parameters were tested and calibrated, see Oosterlo et al. (2019). Next, a test was performed with 100 random run-up levels as derived from the Rayleigh distribution, to be able to assess the performance of the system in measuring the wave run-up and overtopping. After that, the wave run-up simulator was placed under an angle of 45° with the dike normal. With this set-up, obliquely incident waves were generated, see also https://youtu.be/RMyIAh8bU_0. For the first tests with oblique waves, 3 times 6 up-rushing waves were generated (simulator filling levels from 2 m to 7 m, 18 waves in total). During these tests, several different distances between the laser scanner scan lines were tested, being 1.3 m, 2.5 m and 3.4 m. The last test with oblique waves again consisted of 100 randomly generated up-rushing waves, to assess the performance of the system in measuring the oblique run-up and overtopping.

3. Data processing and data analysis

Before the start of the tests, the system had to be calibrated, where the exact positions of the laser scanners and laser lines had to be determined. For the full calibration procedure, refer to Oosterlo et al. (2019). The main step in the data processing procedure consists of converting the measured distances R_1 and R_2 in polar coordinates to cartesian x (horizontal) and z (vertical) coordinates in metre, taking into account the positions and angles of the laser scanners, see Fig. 3. For a full description of the coordinate transformation and data analysis procedures, see Oosterlo et al. (2019). The dry slope was determined from the first 10 s of a test. Next, the run-up depths were determined by subtracting the dry slope from the measured slope at a certain moment. Depths smaller than a threshold value of 0.01 m were removed to remove noise from the signal and prevent the detection of unrealistically high run-up values. Note that this threshold is smaller than what was used in previous research (Cete, 2019; Hofland et al., 2015), and could be used here because of the generally larger run-up depths that occurred during these field tests than with the previous lab flume research. The run-up height could be determined from the resulting run-up depth and RSSI time series by finding the highest location on the slope where $z_{runup} - z_{dry} > z_{threshold}$ and $RSSI_{runup} - RSSI_{dry} > RSSI_{threshold}$, as shown in Fig. 4 for the run-up depth. The check on RSSI is performed to detect water layers that are thinner than the noise level of the direct distance

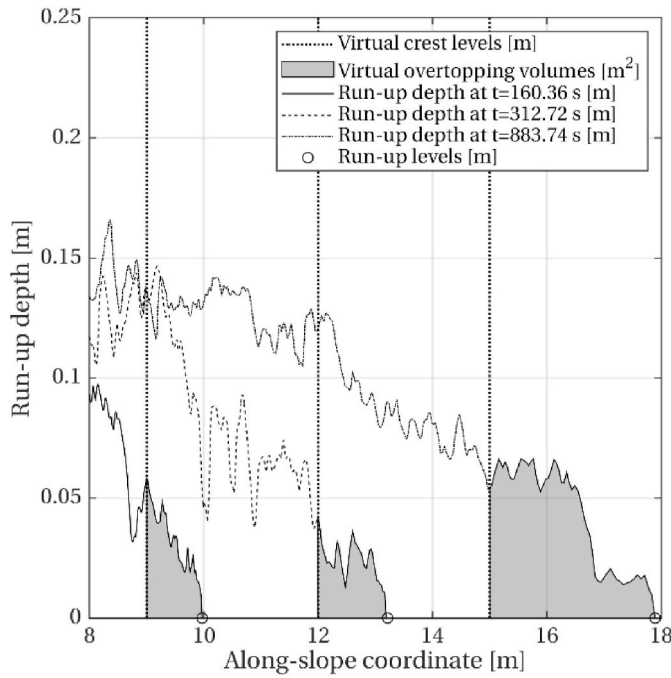


Fig. 4. Determination of run-up levels R_u [m] (circles) and virtual overtopping volumes V [m^3/m] (shaded regions) based on the run-up depths d [m] (solid, dashed and dash-dot lines), for three different waves and at three different virtual crest levels (dotted lines). The waves are plotted for the moment that the volume above the virtual crest line (the shaded area) is maximum for that specific wave. The assumption is that this would be the overtopped volume that would have overtopped if the crest was located at this virtual level.

measurement of the laser scanner.

The front velocities of the up-rushing waves could be determined from the temporal change in run-up level. To this end, first the time signal of the instantaneous front position was smoothed by applying a median filter with a 0.2 s window, followed by a moving average with a 0.6 s window. After that, the time derivative was taken and the maxima were determined, giving the maximum front velocities during each wave. The maximum front velocities were determined from the videos as well; by taking the minimum number of video frames it took the front to travel 1 m on the slope.

The (virtual) wave overtopping volumes and mean discharges could be calculated from the laser data at different virtual crest levels. Fig. 4 shows for three different waves the largest overtopping volume of each wave, at three virtual crest levels. The overtopping volumes were determined by integrating the depicted instantaneous run-up depth above the virtual crest level (shaded areas in Fig. 4). Then, the overtopping volumes were found by taking the maximum values of these volumes during each wave. Hereby it was assumed that these maximum volumes per wave correspond to the actual overtopping volumes. The mean overtopping discharge q , in m^3/s per m width, was found by taking the sum of these peak volumes and dividing by the test duration, $q =$

$\sum_N V_{\text{peak}}/D$, with N [–] the number of waves, V_{peak} [m^3/m] the maximum volumes above the virtual crest level and D [s] the test duration. The virtual overtopping discharge was calculated by multiplying the front velocity time series with the run-up depth time series at several virtual crest heights as well. Here, the assumption was made that the front velocity, which changes in location on the slope, corresponded to the flow velocity at the virtual crest.

Another important step in the data processing procedure was the filtering out of disturbances like rain or a person standing in the laser beam. As described in Oosterlo et al. (2019), using the right laser scanner settings, i.e. the last echo and without any additional filtering,

the influence of such disturbances on the results was small. When the first echo was used during rain, this led to more detection of rain, as the laser beam sometimes reflected off a raindrop. The last echo gave good results during dry conditions and improved the results during rain, as this echo did come from behind the raindrops. Waves were removed from the signal if a person was standing in the laser beam.

The percentage of invalid measurements at a certain location indicates the quality of the measurement. An invalid measurement means that the magnitude of the laser reflection was too small. For all tests, these percentages were very small ($\approx 0.1\%$). Finally, from the accelerometer data, it was determined that the influence of vibrations due to the wind on the data quality was small.

Commonly, the root-mean-square error (RMSE) and the from the RMSE derived normalised root-mean-square error and scatter index are used to evaluate the performance or reliability of some measurement or model. However, Mentaschi et al. (2013) showed that the RMSE and its variants give smaller values for models affected by negative bias. Hence, these indicators are not always reliable to assess the accuracy of models or measurements. They showed that the HH-indicator as proposed by Hanna and Heinold (1985) provides more reliable information on the accuracy of models or measurements. This HH-indicator is used to assess the performance of the laser scanners in the present paper and is defined as:

$$HH = \sqrt{\frac{\sum_{i=1}^N (M_i - O_i)^2}{\sum_{i=1}^N M_i O_i}} \quad (1)$$

where M_i is the i th modelled data, O_i is the i th observation and N is the total number of observations. Furthermore, the Normalised Bias Indicator is used:

$$NBI = (\bar{M} - \bar{O}) / \bar{O} \quad (2)$$

Both the HH and NBI are dimensionless.

4. Results and analysis of perpendicularly incident waves

4.1. Wave run-up heights

The left panel of Fig. 5 shows the run-up heights for a test with perpendicularly incident waves (seven waves, three times repeated) from both laser scanners, and based on both the measured distance R and laser reflectance $RSSI$. The results were plotted against the run-up heights derived from video recordings. Only 15 out of 21 waves are visible, as waves with a simulator filling level of 6 m and 7 m overtopped the dike. The data agree well, with most data within the ± 0.05 m bounds and all except one data point within the ± 0.10 m bounds. The run-up was simulated in a robust manner, as the run-up levels for each set of three waves with the same filling level lie within a few centimetres of one another.

The data of both laser scanners agree well, where laser scanner 2 gave a somewhat larger HH-value relative to the observed data. NBI values were close to zero (< 0.01), being positive for laser scanner 1 and negative for laser scanner 2. Determining the run-up based on the measured distance and $RSSI$ gave almost equal results. This is an improvement compared to what Hofland et al. (2015) and Cete (2019) found, where the $RSSI$ performed better. This can be explained by the lower run-up depth threshold of 0.01 m, which could be used here. The differences that occurred between the laser scanner and video run-up heights arose from the variability over the width of the front of the up-rushing wave. The average run-up height of the front was taken from the videos, but the lasers give the run-up at two distinct locations along the front. Variabilities in the 2% run-up height $R_{u2\%}$ over the width of the flume, excluding wall effects, were on average 7% of the $R_{u2\%}$ for tests in the Delta Flume at Deltares, the Netherlands (Cete, 2019). Although smaller, such oscillations over the width of the front also

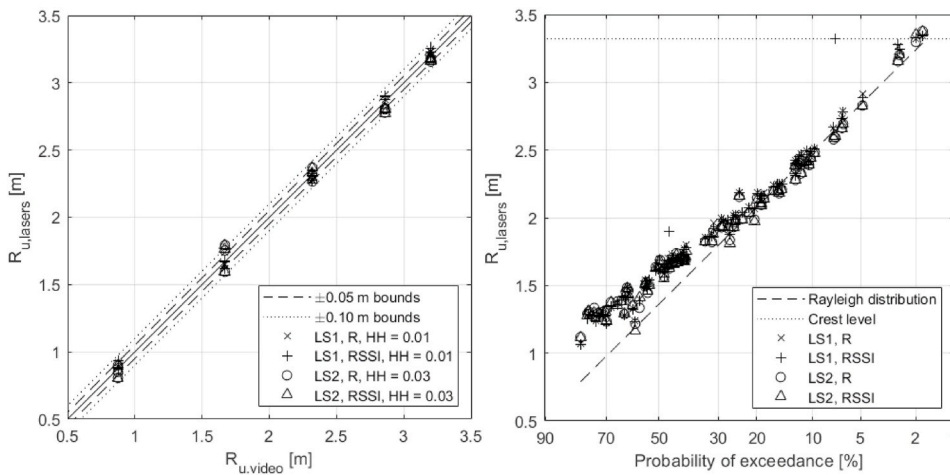


Fig. 5. Left: Run-up heights derived from both laser scanners (LS1 and LS2), based on distance (R) and laser reflectance (RSSI), compared with run-up heights from videos, for a test with 21 perpendicularly incident waves. The HH-indicator values are shown as well. Right: Run-up heights for test with 100 randomly generated perpendicularly incident waves for both laser scanners, as well as Rayleigh distribution derived from wave run-up simulator filling level formula (dashed line). The horizontal axis is plotted on Rayleigh scale, the dike crest level is indicated with the horizontal dotted line.

occurred during the present tests.

The right panel of Fig. 5 presents results for a test with 100 randomly generated perpendicularly incident waves. Of this test, only 81 waves could be used, as a person was standing in the laser beam during the last waves of the test. Since no video recording was available for this test, the laser data were compared against the theoretical run-up heights according to the Rayleigh distribution as simulated by the wave run-up simulator. The run-up simulator generates the wave run-up according to a Rayleigh distribution, which was calibrated based on visual observations of the 3*7 different waves during a calibration test. The dashed line in the right panel of Fig. 5 represents this Rayleigh distribution. The horizontal axis was plotted on Rayleigh scale such that deviations from the Rayleigh scale can easily be recognised. Note that the measurements are no real exceedance plot, as the run-up levels for a certain probability of exceedance were created deterministically. The data agree well with the theoretical Rayleigh distribution for the higher run-up levels, with one outlier in the RSSI values of laser 1. This outlier indicates that for this wave, the measured run-up level based on the RSSI did not agree with the theoretically simulated run-up level as derived from the Rayleigh distribution. The highest few run-up levels also deviate somewhat from the distribution. This can be explained as follows; since the largest waves overtopped the dike, this means that the maximum measured run-up level was the dike crest level (dotted line). The lowest run-up levels were higher than expected according to the Rayleigh distribution as used for the run-up simulation, which was confirmed visually during the

test as well.

4.2. Wave run-up depths

The run-up depth is defined as the water depth of the up-rushing wave at a certain location, see Fig. 3. These run-up depths were measured not only by the laser scanners, but also by five surf boards or floaters. The locations of the surf boards were given in the left panel of Fig. 2. The left panel of Fig. 6 shows the maximum run-up depths of the different waves as measured by the laser scanners at approximately halfway up the slope ($z = 1.42$ m, crosses and circles). Furthermore, the figure shows the depths as measured by the third surf board at this same location (asterisks), and visually estimated run-up depths (diamonds). These visually estimated depths came from hand-held video recordings, by determining the water level at the side boards. The left panel of Fig. 6 also shows the linear equation of Van der Meer (2011) (dashed line):

$$d = c_d(R_u - z) \quad (3)$$

where d [m] is the run-up depth, c_d [–] a coefficient, in this case being 0.25 for a 1:5 slope, R_u [m] the run-up height, and z [m] an arbitrary height on the slope. Note that the line is curved here, since the equation was not plotted against the run-up height, but the corresponding filling levels of the simulator.

Table 1 gives HH and NBI values for the run-up depths, comparing the depths as measured by the different instruments. Reasonable

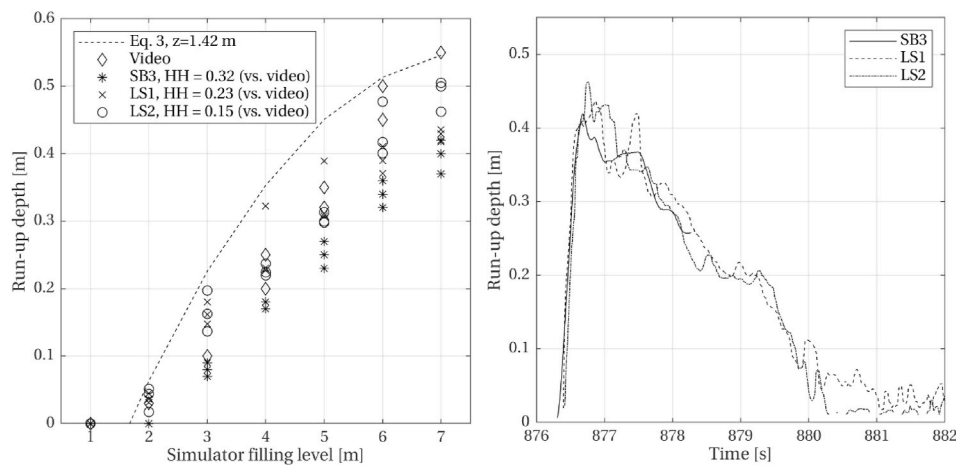


Fig. 6. Left: Run-up depths as measured with both laser scanners (LS1 and LS2), the third surf board (SB3) and as estimated from videos at $z = 1.42$ m, compared with the relation of Van der Meer (2011) (Eq. (3)). Right: Run-up depths in time at the same location for a single wave, for both laser scanners and the third surf board.

Table 1

HH and NBI values, comparing the run-up depths as measured by different instruments. SB3 is the third surf board, LS1 is laser scanner 1, LS2 is laser scanner 2.

Run-up depths		
Instruments	HH [–]	NBI [–]
SB3 vs. Video	0.32	–0.28
LS1 vs. SB3	0.26	0.30
LS2 vs. SB3	0.27	0.33
LS1 vs. Video	0.23	–0.06
LS2 vs. Video	0.15	–0.04

agreement was found between the data, with the largest differences occurring between the surf board and the visually from video estimated values. The laser scanners generally gave larger values than the surf board, but slightly smaller values than the visually estimated ones. This can be explained as follows; the laser scanners scan the surface of the foam, which the surf boards do not. It was observed that the surf boards slightly sink into the water and do not record the smallest run-up depths, explaining the generally smaller values and the zero values for a filling level of 2 m. The visually estimated values were larger for the largest waves. Since the visually estimated depths were determined at the side boards, they might have been slightly overestimated, as most spray also occurred at the side boards. The shape as obtained from the equation agrees quite well, but it overestimates the depths. These trends also hold for locations higher on the slope. Hence, it can be concluded that at this location and higher on the slope, the lasers accurately measure the run-up depths.

Different results were found closer to the simulator. In front of the simulator, larger run-up depths occurred, the water was highly turbulent, and a lot of foam and spray were present. Larger differences between the different measurement techniques were found at those locations. The visually estimated run-up depths were around 0.60 m or 0.65 m in front of the simulator for the largest waves. Due to the mounting, the surf boards could not measure a run-up depth larger than approximately 0.50 m, and thus gave an underestimation close to the simulator. Since the laser scanners measure the foam and spray, this led to overestimations of the run-up depths close to the simulator for the largest waves, where values > 1 m were found.

The right panel of Fig. 6 shows the run-up depth in time for a wave with a simulator filling level of 7 m at the same location on the slope ($z = 1.42$ m), for both laser scanners and the third surf board. The time record agrees quite well, but the lasers again gave a somewhat larger maximum depth. The same holds for the other waves of the test. Note that the surf board signal ends at a depth of approximately 0.25 m. The surf boards need to be lifted out of the water before the run-down starts, as they would break otherwise. Hence, another advantage of the laser scanners is that the whole run-up depth time signal can be measured, including the smaller depths and the run-down.

4.3. Front velocities

Comparing the maximum front velocities based on the laser scanner data with the velocities based on the video analysis, a few outliers were found, but most data points were located within the ± 0.5 m/s bounds. The data points of both laser scanners agree well (HH = 0.08, NBI = 0.02), better than the laser and video data (HH = 0.12, NBI = –0.05), but overall the deviations were small. The deviations that did occur can be explained by the limited framerate of 30 fps of the videos, which led to less accurate results for larger front velocities.

Front velocities were determined from the paddle wheel records as well, by determining the time it took the front to travel on the slope from one paddle wheel to the next. See the left panel of Fig. 2 for the paddle wheel locations. The velocity was determined by dividing the travelled distance by this measured time delay. Hence, the paddle wheels were

used as wave detectors. Such front velocities were determined from the laser data and videos as well. The left panel of Fig. 7 plots these laser data against the video and paddle wheel data. The data agree quite well, with most data within the ± 0.5 m/s bounds and the data of all but one wave within the ± 1 m/s bounds, giving confidence in the laser analysis and results. The data of both laser scanners agree well (HH = 0.07, NBI = 0.01), the same agreement as was found between the video and paddle wheel data (HH = 0.07, NBI = 0.01).

The right panel of Fig. 7 gives the run-up and front velocity time signals of one of the laser scanners and the front velocity time signal from the manual video analysis for one wave. Both the development in time and the maximum front velocity for both techniques agree well. The dotted vertical lines indicate percentages of the maximum run-up level. According to Van der Meer (2011), front velocities close to the maximum front velocity are found between 15% and 75% of the maximum run-up level, being approximately constant in this range. The actual maximum front velocity is reached between 30% and 40% of the maximum run-up level. Here, the highest front velocities indeed occurred within the range of 15%–75% of the maximum run-up level. However, the actual peak of the front velocity was reached at around 50% of the maximum run-up level for this case. The same behaviour was found for the other waves of this test. This difference in location of the peak front velocity can be explained as follows; the analysis of Van der Meer (2011) was based on real waves instead of waves generated by the wave run-up simulator. Despite this deviation in peak front velocity location, the wave run-up simulator seems to simulate the development of the front velocity of a wave properly, and the laser scanners can be used to locate the front velocity over the slope automatically and accurately.

4.4. Wave overtopping volumes and discharges

The left panel of Fig. 8 shows the overtopping discharges as determined based on both maximum volumes above the virtual crest and run-up depth multiplied with front velocity (see section 3) for the test with 100 randomly generated waves, and compares them with the EurOtop (2018) wave overtopping equations. 81 out of 100 waves of this test could be used, due to a person standing in the laser beam.

The discharges based on the maximum volumes above the virtual crest agree well with the EurOtop (2018) equations. Cete (2019) and Hofland et al. (2015) achieved good results for wave flume tests, by determining the overtopping using this method. However, the method had not been applied to an actual dike before. Results based on run-up depth multiplied with front velocity lie mainly within the 90% bounds of the overtopping equations, but deviate from the mean line. This overestimation mainly stems from the assumption that the front velocity around the virtual crest equals the flow velocity at the virtual crest. Since the results based on maximum volumes performed better, this method is recommended for future research.

The virtual overtopping volumes are similar to, but not the same as overtopping volumes as measured by a tank. With the virtual volumes, a pressure gradient from the run-up volume above the virtual crest is present still, which would not be present with an overtopping tank. Despite these differences, still good results were achieved here based on the maximum virtual volumes. Furthermore, the results agree well with the equations, despite the fact that these results were based on only 81 waves. Overtopping discharges are usually based on much larger numbers of waves. The results show that the simulator apparently simulates the correct overtopping volumes and discharges, even though the wave run-up simulator is calibrated on run-up levels and not on overtopping volumes or discharges.

Both laser scanners gave almost equal results. Only for the largest virtual crest freeboards slight differences occur, because these discharges were based on only a few waves. As mentioned before, variability in the run-up height over the width of the test section occurred. If a wave surpassed the virtual crest level at the scan line of laser scanner 1,

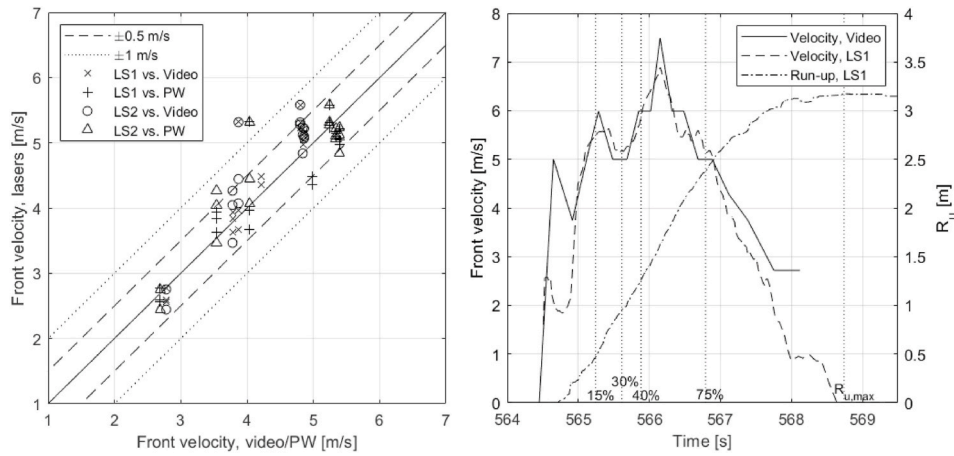


Fig. 7. Left: Front velocities determined from laser scanner data versus paddle wheel (PW) and video data. Velocities based on front travelling from one paddle wheel to the next. Right: Run-up (dash-dot) and front velocity (dashed) time signals of laser scanner 1 and front velocity time signal (solid line) from video analysis for a single wave. The dotted vertical lines indicate percentages of the maximum run-up level.

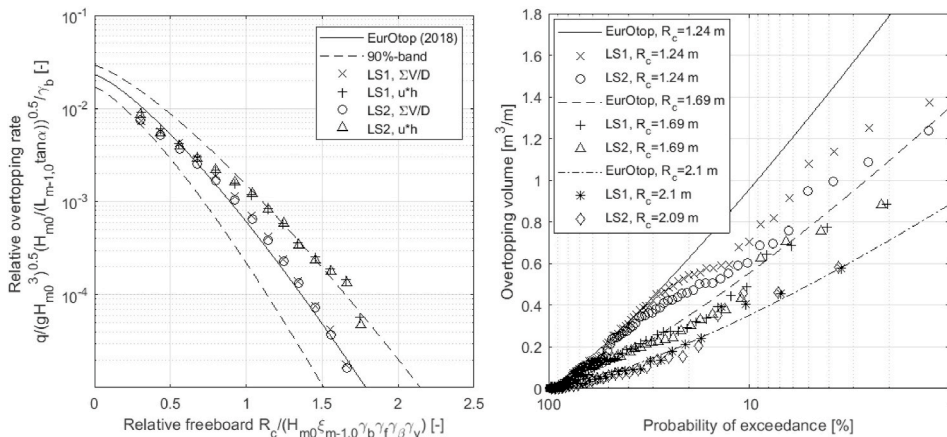


Fig. 8. Left: Relative overtopping rate at different virtual crest heights based on maximum volumes (crosses, circles) or run-up depth multiplied by front velocity (pluses, triangles) for a test with 100 random perpendicularly incident waves, compared to EurOtop (2018) equations (solid and dashed lines). Right: Distribution of overtopping volumes for three different crest freeboards, compared to EurOtop (2018). R_c [m] is the crest freeboard, $\xi_{m-1,0}$ [-] the breaker parameter, the different γ [-] parameters are influence factors, see EurOtop (2018).

but only barely reached the virtual crest at the scan line of laser scanner 2, this quickly results in a different mean overtopping discharge for these large freeboards. The slightly smaller discharges that were found for the lowest crest freeboards were likely caused by the fact that only simulator filling levels larger than 0.7 m were simulated, which means that the smallest waves were omitted. These smallest waves would contribute to the overtopping discharge for these small freeboards in reality.

The right panel of Fig. 8 compares the distributions of virtual overtopping volumes with the EurOtop (2018) equations, which give the overtopping volume for a certain probability of exceedance, for three different freeboards. The volumes agree reasonably well for the medium and high crest levels. For the lower crest level, the results also agree reasonably well for the larger probabilities of exceedance, but for the smaller probabilities (larger volumes) the measured volumes were smaller than according to the equations. For these small freeboards, a large virtual overtopping volume means that a large run-up depth was present over a large area of the slope. If there was any bias or error in the depths as determined by the laser scanners, this bias starts to weigh stronger for these large volumes and small freeboards, because of the large surface that is integrated. The previously mentioned pressure gradient and the run-down, which do not occur with an overtopping tank, could also have influenced the results. Finally, the limited number of waves that were simulated could have played a role.

5. Analysis and preparation for obliquely incident wave measurements

The laser setup will be employed in an area with very oblique wave attack. Waves during storms are expected to arrive at angles up to 80° to the dike normal. By using two parallel laser lines, the time lag between the two measurements can give information about the obliquity of the wave attack. This section explores the possibilities of this system. The first part evaluates the first tests with the system on artificially generated oblique transient flows (waves) by the wave run-up simulator. This flow is thought to have some (but not all) characteristics similar to actual oblique waves. Therefore, it can be assessed if the time lag and corresponding shore-parallel front velocity can be obtained from these signals. The second part considers synthetic measurements, made by taking two virtual laser scanner scan lines from simulations with the numerical wave model SWASH. Based on these simulations, it is examined which characteristics of oblique waves can be obtained from the virtual laser signals. These synthetic measurements can then be compared to the exact quantities as calculated by the model. The section ends with the optimisation of the laser scanner system for future measurements in the field, during storms with oblique wave attack.

5.1. Tests with oblique waves generated by the wave run-up simulator

5.1.1. Wave run-up heights

First, the wave run-up heights as measured by the laser scanners are

compared with video observations, for oblique waves generated by the run-up simulator (see the right panel of Fig. 1). This is done in order to check if the laser scanners can measure the run-up heights of these oblique waves correctly. Fig. 9 shows the run-up heights for a test where six 45° oblique waves were repeated three times, for both laser scanners and plotted against the run-up heights derived from videos. The same trends were found as for the perpendicularly incident waves. The data agree well, with most data within the ± 0.05 m bounds, and all but two data points within the ± 0.10 m bounds. Here, both laser scanners gave the same HH value relative to the visually observed data, see the legend of Fig. 9, and NBI values of approximately -0.01 . The differences that did occur between the lasers and video were caused mainly by the interpolation of the visually observed run-up levels between the vertical grid lines that were painted on the grass slope where the run-up was observed, see the right panel of Fig. 1. The laser lines were located in between these vertical grid lines.

5.1.2. Time lag and shore-parallel front velocities

Long-crested obliquely incident waves result in a sinusoidal wave propagating along the length-axis of the dike. Actual storm waves are short-crested at the location of interest, and result in complex wave fronts. During the oblique wave tests with the simulator, it was observed that even though the waves from the simulator did all come from the same direction, as with long-crested waves, the simulator was not wide enough to simulate oblique wave attack over a sufficiently large surface. The volume of water that was released from one point was not the same as a wave crest travelling unaltered along the dike, but more akin to a jet or bore. Hence, the oblique waves as generated by the simulator do not correspond to actual obliquely incident short-crested waves. However, the flow as generated by the simulator is thought to have some characteristics similar to actual oblique waves. During actual storms in the area, sometimes jets or bores occurred that mainly propagated along the length-axis of the dike as well. Such jets were caused by very obliquely incident breaking waves. These jets do roughly correspond to the oblique waves as generated by the simulator. Therefore, it can be assessed if the time lag and corresponding shore-parallel front velocity of these waves can be obtained from the laser scanner signals. The run-up depths

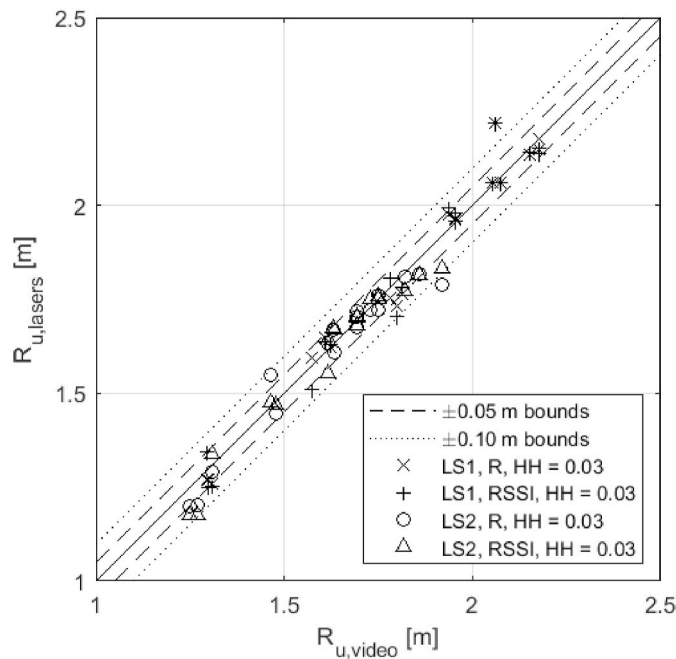


Fig. 9. Run-up heights from both laser scanners, based on both measured distance (R) and laser reflectance ($RSSI$) versus run-up heights from videos, for a test with obliquely incident waves. Distance between laser lines 1.3 m.

and overtopping discharges will not be considered further here, since no validation data were available.

It was possible to determine the time lag in the laser scanner signals. The left panel of Fig. 10 shows an example of the time lag in the laser scanner signals for one wave. The shore-parallel front velocities (along the y-axis in Fig. 3) could then be determined from these time lags and the distance between the scan lines. The right panel of Fig. 10 compares the maximum shore-parallel front velocities based on the laser scanners to video observations for all 18 waves of one oblique test. The results agree reasonably well, with one outlier in the laser scanner data. The HH between laser and video results is 0.13, the NBI is 0.002. The differences that occur are caused mostly by the limited 30 fps framerate of the videos. The maximum velocities of the higher filling levels are approximately equal. Apparently, the simulator generates these larger waves with an approximately constant shore-parallel velocity. Thus, the time lags between the laser signals can potentially be used to determine the shore-parallel velocities of such jets during actual storms in the field.

5.2. Numerical SWASH simulations

This section considers the simulations performed with the numerical wave model SWASH. These simulations are used to examine which characteristics of oblique waves can be obtained from synthetic measurements with two virtual laser scanner scan lines. The studied characteristics are the wave peak period, the wave angle of incidence and the wave overtopping discharge. These synthetic measurements can then be compared to the exact quantities as calculated by the model. Finally, the obtained results are used to determine the ideal distance between the laser scanner scan lines. For these simulations, a rectangular basin was used, with dimensions of 100 m cross-shore and 300 m alongshore, and grid cell sizes ranging between 0.10 m and 0.20 m. The waves entered the domain from the west, and either a vertical wall (full reflection) or a 1:4 dike slope (partial reflection) was located at the eastern boundary. The northern and southern boundaries were absorbing and located far enough from the area of interest such that boundary effects did not influence this area of interest. Tests were done for water depths of 10 m and 2.5 m. Both monochromatic waves and irregular short-crested wave fields were applied. Monochromatic waves were chosen, since the analysis method was derived based on monochromatic waves, see section 5.2.1. The irregular short-crested waves were used, since such conditions represent the conditions at the location of interest, the Eems-Dollard estuary. (Significant) incoming wave heights were set to 1 m, the (peak) period was set to 4 s, angles of incidence ranged from 15° to 60°, roughly corresponding to yearly storm conditions in the area of interest. The irregular wave field was characterised by a standard JONSWAP spectrum (Hasselmann et al., 1973), with a directional spreading of 25°.

Table 2 gives an overview of the SWASH simulations that were performed. Water depth output was obtained along 5 virtual laser scan lines with an output frequency of 50 Hz, at distances of 1 m, 2 m, 4 m and 8 m from the first line, corresponding to the characteristics of the actual laser measurements. On the dike slope, this water depth output is the same as the run-up depth as measured by the laser scanners. Furthermore, for some of the cases discharge output q [$\text{m}^3/\text{s}/\text{m}$] (q -parameter in SWASH, integral of positive flux at a certain virtual crest level) was obtained at several virtual crest levels. Finally, for three cases a (virtual) overtopping box was built into the model for further analysis of the overtopping discharges. The left panel of Fig. 11 presents part of the 2.5 m deep basin with a dike slope, with the virtual laser lines indicated as well. Refer to <https://youtu.be/cy-VWmV7aUA> for an example wave field, of which the right panel of Fig. 11 gives a snapshot.

5.2.1. Data analysis

The time lag between both laser scanner signals was shown in Fig. 10. From this time lag between the two laser signals, the angle of incidence can be obtained. Fig. 12 shows this schematically, providing the definitions for the analysis method. The solid lines represent an

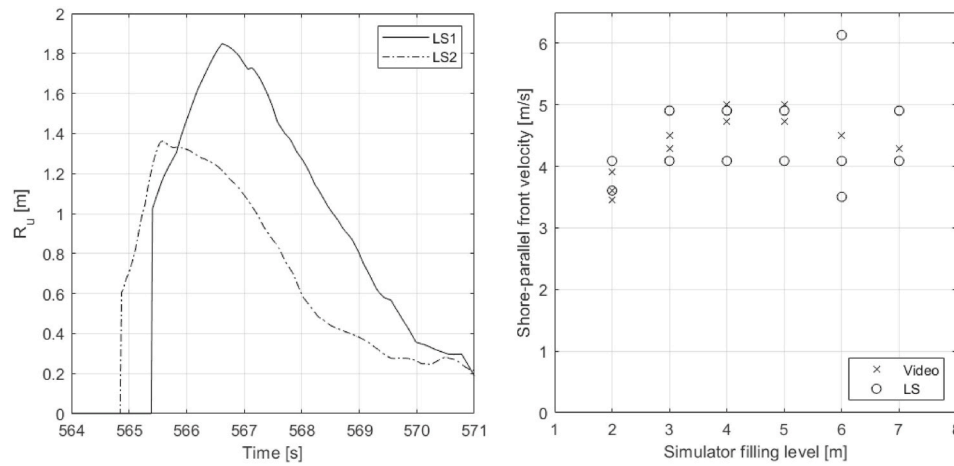


Fig. 10. Left: Snapshot of run-up level in time for both laser scanners during oblique wave attack. The time lag and different maximum run-up levels are visible. Right: Maximum shore-parallel front velocities determined from laser scanner data (circles) versus video data (crosses). Laser velocities based on the time lags between the laser scanner signals. Distance between laser lines 2.5 m.

Table 2

SWASH calculations that were performed. Angles of incidence β ranging from 15° to 60° , (significant) wave height $H_s = 1$ m for all tests, wave (peak) period $T_p = 4$ s for all tests.

Test no. [–]	Water depth [m]	Boundary type [–]	Wave boundary condition [–]	Angle of incidence β [°]
1	10	Vertical wall	Monochromatic	15
2	10	Vertical wall	Monochromatic	45
3	10	Vertical wall	Monochromatic	60
4	2.5	Vertical wall	Monochromatic	15
5	2.5	Vertical wall	Monochromatic	45
6	2.5	Vertical wall	Monochromatic	60
7	2.5	Slope	Monochromatic	15
8	2.5	Slope	Monochromatic	45
9	2.5	Slope	Monochromatic	60
10	2.5	Slope	JONSWAP	15
11	2.5	Slope	JONSWAP	35
12	2.5	Slope	JONSWAP	45

obliquely incident sinusoidal wave, with the wave direction indicated by the arrow, propagating towards the dike, with a phase velocity c [m/s] and a wavelength L [m]. The dike toe and crest are indicated with the thick solid lines. This wave causes a projected wave to travel along the dike, with a velocity c' [m/s] and a wavelength L' [m] (dashed lines). This projected wave is sampled at the two locations LS1 and LS2 (dotted lines), at a distance D [m] from one another.

From the numerical simulations, the run-up was determined in the

same way as for the actual laser scanner measurements, by determining the highest location on the slope where the run-up depth was larger than zero. The first step in the further analysis is to determine variance density spectra from the run-up signals of the (virtual) laser scanners, with finite and discrete Fourier transforms (e.g. Bendat and Piersol, 1971):

$$X_j(f, N\Delta t) = \sum_{n=1}^N R_{u,j}(n\Delta t) e^{-i2\pi f n \Delta t} \quad (4)$$

with $R_{u,j}$ ($j = 1, 2$) [m] the run-up time signals for the scan lines, f [Hz] the frequency, Δt [s] the sampling interval, n integers and N the window length in samples. Next, the auto-spectral density is determined:

$$S_{jj}(f) = \frac{2}{N\Delta t} E[|X_j(f, N\Delta t)|^2] \quad (5)$$

with $E[\cdot]$ being an ensemble average over the number of windows. Since these spectra are based on the run-up time series, they do not represent a real wave spectrum, from which e.g. a wave height can be determined. However, from the peak(s) of these spectra, the wave peak frequency f_p [Hz] can be determined. After that, the cross-spectral density is determined from both run-up signals for each pair of virtual laser lines at different distances from one another (1 m, 2 m, 4 m and 8 m apart):

$$S_{12}(f) = \frac{2}{N\Delta t} E[X_1^*(f, N\Delta t) X_2(f, N\Delta t)] \quad (6)$$

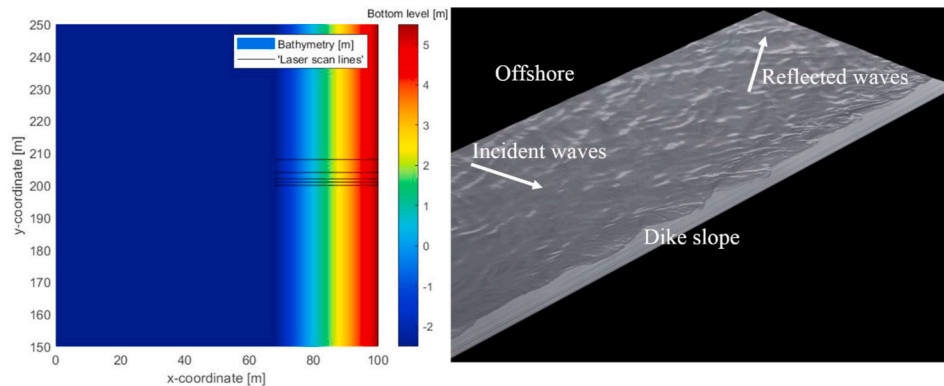


Fig. 11. Left: Part of the 2.5 m deep SWASH basin with a 1:4 dike slope. The virtual laser scan lines are indicated as well. Right: Snapshot of irregular directional wave field, with an angle of incidence of 45° and a directional spreading of 25° . Also refer to <https://youtu.be/cy-VWmV7aUA>.

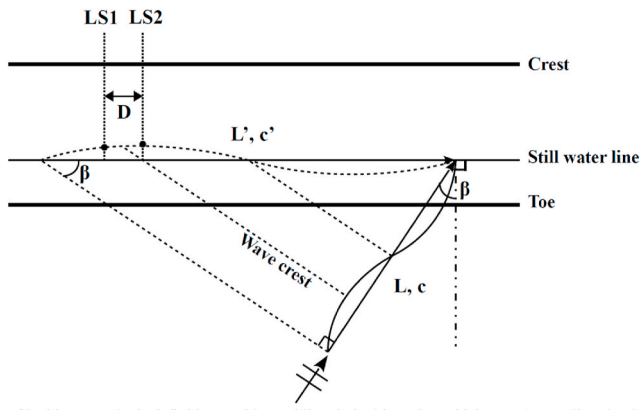


Fig. 12. Angle of incidence analysis definitions, with an obliquely incident sinusoidal wave (wave direction indicated by the arrow) propagating towards the dike (toe and crest indicated with thick solid lines), with a phase velocity c and a wavelength L . This wave causes a projected wave to travel along the dike, with a velocity c' and a length L' (dashed lines). β is the angle of incidence. Laser scanner scan lines indicated by the dotted lines (LS1 and LS2), with a distance D between them.

with X^* the complex conjugate of X . All previous equations in this section are defined for $0 < f < 1/\Delta t$. Martins et al. (2016) used a similar approach to determine wave peak periods and celerities based on data as measured by a single laser scanner. The ‘time lag spectrum’ $\zeta(f)$ is obtained from the cross-spectrum at each frequency, as follows:

$$\zeta(f) = \frac{\text{Arg}(S_{12}(f))}{2\pi f} \quad (7)$$

From the spectrum of time lags between these virtual laser scanners and the distance between both laser lines D , the phase velocity of the projected waves can be determined at each frequency:

$$c' = \frac{D}{\zeta(f)} \quad (8)$$

Next, the incoming wave celerity c is determined at each frequency according to linear wave theory. Finally, the ‘angle of incidence spectrum’ β can be found with trigonometry, see Figs. 12 and 13:

$$\beta = \sin^{-1} \frac{c}{c'} \quad (9)$$

E.g. the peak angle of incidence can then be determined by taking the angle of incidence corresponding to the peak frequency from the angle of incidence spectrum, see Fig. 13.

The method above was based on monochromatic, sinusoidal waves in deep water, whereby it was assumed that the wave angle of incidence is the same as the angle of the breaking wave on the slope. Next, it will

be assessed whether the method performs well for realistic wave conditions of increasing complexity.

5.2.2. Wave (peak) periods

Table 2 gives the SWASH simulations that were performed. The wave peak periods were determined from the auto-spectral densities of the run-up signals (Eq. 5) and compared to the wave peak period of 4 s as applied in SWASH. The overall deviations were very small ($HH = 0.006$, $NBI = 0.01$). Hence, with this method a good prediction of the incoming wave period can be determined with a laser scanner, without additional measurements offshore.

5.2.3. Angles of incidence

The angle of incidence spectra (Eq. (9)) give the angle of incidence for each mode in the spectrum of the measured run-up. Fig. 13 gives example variance density spectra and angle of incidence spectra of a monochromatic and an irregular short-crested case. Peak angles of incidence are indicated with a circle. Fig. 14 shows these estimated peak angles of incidence as determined from the virtual laser run-up data for all SWASH simulations. The figure compares them with the modelled angles of incidence.

Generally, the angle of incidence results showed a more constant trend over the entire frequency domain for the monochromatic cases than for the JONSWAP cases. The left panel of Fig. 13 seems to show larger angles of incidence for the lower frequencies, but note that no energy is present outside the peak frequency. Hence, this likely arose from the data analysis, and was not a physical phenomenon. Around the peak frequency, the angle of incidence lies quite close to the modelled 15° , thus being reliable. The right panel of Fig. 13 shows more scatter, caused by the shallow water depth and directional spreading of the waves. Larger deviations were expected for the more complex cases, as the analysis method was based on deep water, unidirectional and monochromatic waves. Another likely cause is that the analysis method was based on the assumption that the wave angle of incidence is the same as the angle of the breaking wave on the slope, which could differ somewhat in reality. However, as for the monochromatic case, around the peak frequency a more constant trend occurs, with the estimated angles of incidence quite close to the modelled angle of incidence of 35° . Similar trends were found for the other simulations as well.

The left panel of Fig. 14 compares the estimated angles of incidence with the modelled ones. The data agree quite well, with most values within the $\pm 5^\circ$ error bounds and all values within the $\pm 10^\circ$ bounds. The results for a water depth of 10 m, a vertical wall and monochromatic waves agree very well ($HH = 0.05$, $NBI = 0.02$). This can be explained by the fact that the analysis method was based on such conditions as well. The HH and NBI values show that generally larger deviations were found with increasing complexity of the modelled conditions. These larger

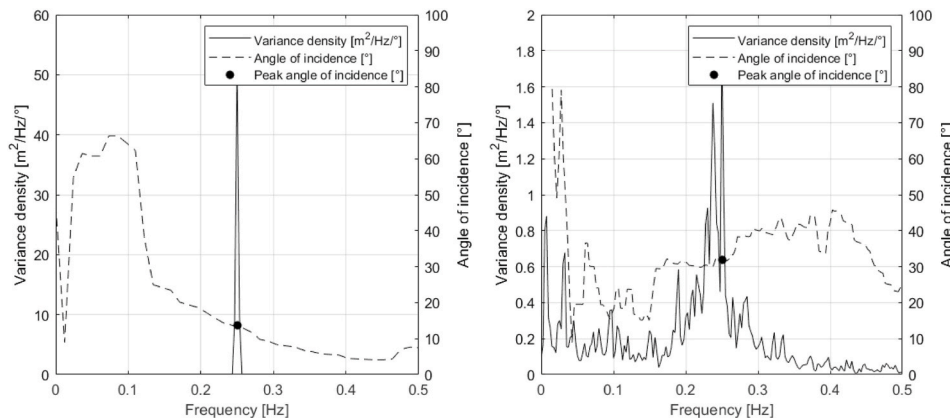


Fig. 13. Variance density spectra (solid lines) based on virtual laser line run-up data and angle of incidence spectra (Eq. (9), dashed lines) for two cases. Left: Angle of incidence of 15° , water depth of 10 m, a vertical wall and monochromatic waves. Right: Angle of incidence of 35° , water depth of 2.5 m, 1:4 dike slope and irregular, short-crested waves. The angle of incidence spectra give the angle of incidence for each mode in the spectrum of the measured run-up. The angle of incidence β was defined according to Fig. 12. Peak angles of incidence indicated by the circles.

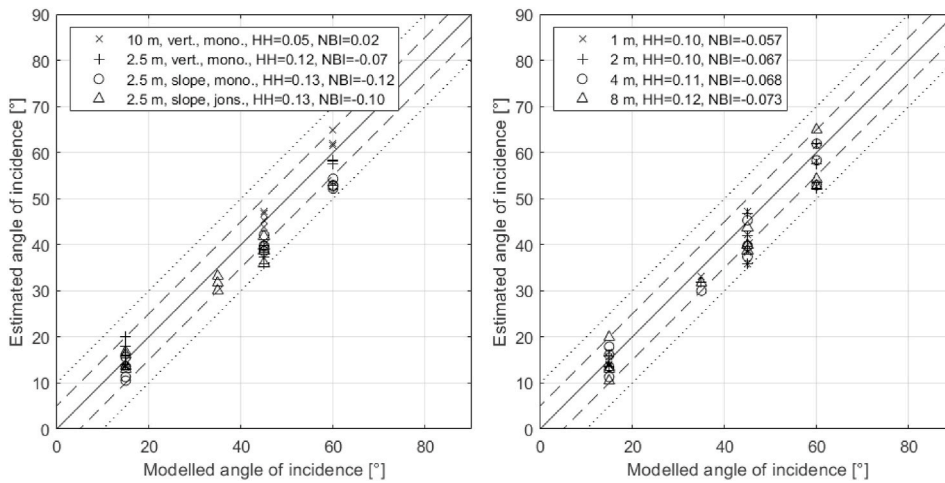


Fig. 14. Wave angle of incidence data for all SWASH simulations, comparing peak angles of incidence as modelled by SWASH with peak angles of incidence derived from virtual laser scanner data (see Fig. 13). Left: Data grouped according to simulation conditions (water depth 10 m or 2.5 m, vertical wall or 1:4 slope, monochromatic or irregular waves). Right: Data grouped according to distance between the scan lines (1 m, 2 m, 4 m or 8 m). HH and NBI values, and $\pm 5^\circ$ and $\pm 10^\circ$ error bounds (dashed and dotted lines) given as well.

deviations mainly arose from the shallower water depth.

Hence, the method determines the angle of incidence at the peak frequency quite well. The performance could potentially be further improved by lengthening the simulation time, thus obtaining longer timeseries and increased statistical reliability. With this method, an estimate of the incoming peak wave direction could theoretically be determined from the cross-correlation between the two run-up signals, without additional measurements offshore. However, further validation in the field is still recommended.

5.2.4. Wave overtopping discharges

The mean wave overtopping discharges were determined from the virtual SWASH laser lines in the same way as for the actual laser scanner measurements, by determining the maximum volumes above several virtual crest levels by integrating the run-up depths above these crest levels. These overtopping discharges were then compared to the SWASH discharge output parameter q , and to the overtopping discharge as determined from the virtual overtopping box in the model.

Fig. 15 shows the results for three JONSWAP cases, being tests 10 to 12, with angles of incidence of 15° , 35° and 45° . The agreement between the virtual laser data, the virtual overtopping box and the SWASH output parameter q is important, as agreement between these three shows

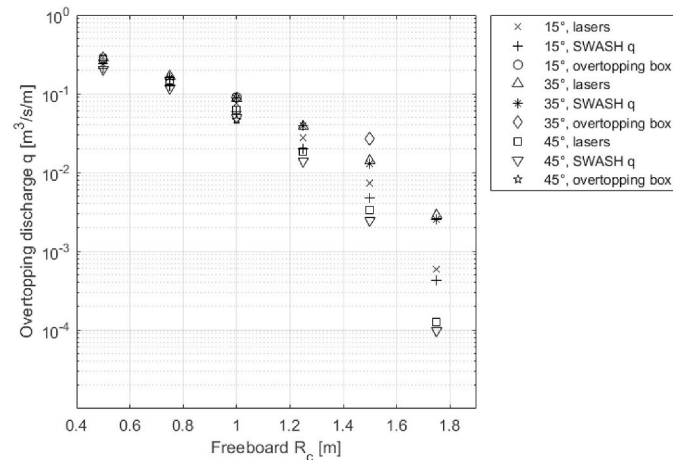


Fig. 15. Overtopping discharge for several virtual crest levels as determined from the virtual laser scanner data for three SWASH simulations. Tests 10 to 12, with angles of incidence of 15° (crosses), 35° (triangles) and 45° (squares). SWASH discharge parameter q (pluses, asterisks, down-pointing triangles) and virtual overtopping box data (circles, diamonds, pentagrams) plotted as well. Simulations with a 1:4 slope, a JONSWAP spectrum with $H_s = 1$ m and $T_p = 4$ s.

consistency and reliability of the method used to determine the overtopping discharge from the laser data. This is the case here, since data from all three methods lie quite close to one another. The virtual laser results and the SWASH output parameter q results agree well. The overtopping box results, which were determined at only one crest level, deviate slightly more, but still agree quite well. Hence, the method as used to determine the mean overtopping discharges from the laser data, by integrating run-up depths and determining maximum volumes above the virtual crest, can be considered reliable and consistent with the SWASH q parameter and virtual overtopping box results. Therefore, the method is considered reliable enough to be used with field data from actual storms with oblique wave attack.

5.2.5. Preferred distance between laser scanner scan lines

Finally, the preferred distance between the laser lines can be determined, based on the previous analyses of front velocities, wave peak periods, angles of incidence and overtopping discharges. This preferred distance can then be used for future measurements with the system in the field, during actual storms with oblique wave attack.

Around the Nyquist frequency, here $f_{Nyq} = 1/2\Delta t = 25$ Hz, large errors are made when determining a spectrum. Generally, it is recommended to choose the Nyquist frequency four times larger than the mean frequency (e.g. Holthuijsen, 2007). Hence, the minimum wave period that can be measured with the laser scanners lies around 0.16 s. This minimum wave period lies past the wind waves regime. Thus, this is not really a limitation, as wind waves will be measured with the system.

Furthermore, a balance between the distance between the laser scanner scan lines and the wave period can be derived, based on the aliasing effect. To be able to distinguish the actual wave frequency of a wave passing by the laser scanners, the distance between the laser lines needs to be smaller than $1/4$ of the projected wavelength L' (with $1/2L'$ or L' , the frequency would not be uniquely defined):

$$D_{lasers} \leq 1/4L' \text{ or } L' \geq 4D_{lasers} \quad (10)$$

$$D_{lasers} \leq L/(4 \cos \alpha) \text{ or } L \geq \cos \alpha \cdot 4D_{lasers} \quad (11)$$

From these relations, the maximum distance between the laser scanner scan lines can be determined, to be able to properly measure a certain wave with a certain frequency. As an example, a wave period of 4 s, a water depth of 2.5 m and an angle of incidence of 45° would result in a maximum distance between the laser lines of approximately 7 m.

2.5 m distance between the laser lines (HH = 0.13, NBI = 0.002) outperformed 1.3 m (HH = 0.14, NBI = -0.017) and 3.4 m (HH = 0.22, NBI = -0.052) between the laser lines in estimating the shore-parallel component of the front velocity of the oblique jets as generated by the wave run-up simulator. The scan frequency of 50 Hz is probably the

limiting factor for the smaller distance between the laser lines. The limiting factor for the larger distance between the laser lines is a change in the front velocity (and direction) that may occur in between the laser lines.

The estimation of the wave (peak) period does not directly depend on the distance between the laser lines. Hence, no clear preference for an ideal distance between the laser lines could be determined from the wave period results.

The right panel of Fig. 14 compares the estimated angles of incidence with the modelled ones by SWASH, grouped according to distance between the virtual scan lines. Only small differences were found between the different scan line distances. Overall, 1 m and 2 m distance performed best, with 1 m slightly outperforming 2 m. However, 2 m distance performed best for the JONSWAP cases, the most realistic cases, with $HH = 0.08$ and $NBI = -0.08$. The JONSWAP conditions simulated here roughly correspond to the conditions in the area of interest, the Eems-Dollard estuary. Furthermore, 2.5 m distance between the laser lines performed best for the determination of the shore-parallel component of the front velocity. Therefore, 2 m distance between the laser lines is recommended as the distance for further measurements in the area.

At other locations, the ideal distance might be different. As a rule of thumb for the distance between the laser scanners, $L_p/16$ could be used, with L_p [m] the local peak wavelength at the toe of the structure, but ideally further research should be performed for such cases.

6. Conclusions

This paper presents the implementation of an innovative system to measure wave run-up and calculate wave overtopping for both perpendicularly and obliquely incident waves, using two coupled laser scanners at a field site. Furthermore, the system can determine the run-up depths and front velocities. Additionally, from the measured run-up signals, the wave (peak) period can be determined, and a reasonable estimate can be given of the wave angle of incidence at the peak frequency. The paper describes the first calibration tests with the system, with perpendicular and oblique run-up generated by the wave run-up simulator on the grass slope of a dike, as well as numerical simulations with the phase-resolving numerical wave model SWASH to assess the set-up for synthetic but realistic oblique wave attack in more detail.

The measured run-up heights agreed well with the visually observed run-up, for both perpendicularly and obliquely incident waves. Differences of only a few centimetres were found, both for the run-up based on measured distance and based on laser reflectance.

Run-up depths were measured reliably with the laser scanners, at locations higher on the dike slope. Closer to the simulator, the lasers gave too large and unreliable depths due to foam, spray and large turbulence. The advantage compared to the generally used surf boards is that the depth can be determined over the whole slope, not just at a few locations.

Front velocities of perpendicularly incident waves could accurately be determined from the laser scanner data. The shore-parallel velocity component could be determined reasonably well from the time lag between the laser signals for oblique waves as generated by the simulator. However, further research in the field is recommended.

The overtopping discharges based on maximum volumes agreed well with the EurOtop (2018) equations for perpendicularly incident waves. The discharges based on run-up depths multiplied with front velocities did not agree as well, although with most values within the 90% bounds of the overtopping equations.

To gain more insight in the potential performance of the system during actual oblique wave attack during a storm, numerical simulations were performed, modelling virtual laser scanner scan lines. The method employed here to determine the overtopping discharge, by integrating the run-up depth and determining maximum volumes above the virtual crest, was compared to the SWASH-model discharge output parameter q

and a virtual overtopping box built into the model, and can be considered consistent and reliable.

From the virtual laser scanner run-up signals, the incoming wave (peak) period could also be accurately determined. Furthermore, from the cross-correlation between the two run-up signals, a reasonable estimate of the wave angle of incidence at the peak frequency could be determined. Determining these parameters from the run-up signals could alleviate the need of additional measurements offshore. However, measurements of the wave height remain necessary and further validation in the field is required.

For the cases considered here, the wave run-up and run-up depths could be determined as accurately with the laser scanner system as with the conventionally used methods. An advantage of the system is that more insight is gained into certain parameters than with the conventional measurement techniques, e.g. into the depths and velocities, which are measured with high resolution. Since the system is mobile, it can measure at several dike locations by moving the system every few years.

The preferred distance between the laser lines was determined as $L_p/16$, being 2 m for the expected conditions in the Eems-Dollard estuary. Since this calibration was successful, the system will now be placed on the dike in the Eems-Dollard estuary to measure oblique wave run-up and overtopping during severe winter storms for the next 3 years, additional to the measurements with overtopping tanks. The expectation is that measuring during storms and validation with data from the overtopping tanks will lead to new insights in and guidelines on the influence of oblique wave attack on wave overtopping.

Author credit statement

Patrick Oosterlo: conceptualisation, methodology, software, validation, formal analysis, investigation, data curation, writing – original draft, writing – review & editing, visualisation, project administration.

Bas Hofland: conceptualisation, methodology, software, validation, writing – review & editing, visualisation, supervision.

Jentsje W. van der Meer: conceptualisation, methodology, validation, investigation, resources, writing – review & editing, supervision, project administration, funding acquisition.

Maarten Overduin: methodology, software, formal analysis, investigation, resources, writing – review & editing.

Gosse Jan Steendam: methodology, investigation, resources, writing – review & editing, supervision, project administration, funding acquisition.

Declaration of competing interest

The authors declare that they have no known competing financial interests or personal relationships that could have appeared to influence the work reported in this paper.

Acknowledgement

This study was made possible by the inspiring input of the late Gerbrant van Vledder. This paper was immensely improved by his knowledge, dedication and guidance. We would like to thank the POV Waddenzeedijken for the use of the wave run-up simulator, as well as Gerben van der Meer, Jan Bakker and Frans Roorda for their help with the wave run-up tests. This study was supported by Waterschap Noorderzijlvest and the Hoogwaterbeschermingsprogramma.

Appendix A. Supplementary data

Supplementary data to this article can be found online at <https://doi.org/10.1016/j.coastaleng.2021.103915>.

References

- Allis, M.J., Peirson, W.L., Banner, M.L., 2011. Application of lidar as a measurement tool for waves. In: The Twenty-First International Offshore and Polar Engineering Conference. <https://onepetro.org/conference-paper/ISOPE-I-11-402>.
- Almeida, L.P., Masselink, G., Russell, P.E., Davidson, M.A., 2015. Observations of gravel beach dynamics during high energy wave conditions using a laser scanner. *Geomorphology* 228, 15–27. <https://doi.org/10.1016/j.geomorph.2014.08.019>.
- Bendat, J.S., Piersol, A.G., 1971. *Random Data Analysis and Measurement Procedures*. John Wiley & Sons.
- Blenkinsopp, C.E., Mole, M.A., Turner, I.L., Peirson, W.L., 2010. Measurements of the time-varying free-surface profile across the swash zone obtained using an industrial LIDAR. *Coast Eng.* 57 (11–12), 1059–1065. <https://doi.org/10.1016/j.coastaleng.2010.07.001>.
- Blenkinsopp, C.E., Turner, I.L., Allis, M.J., Peirson, W.L., Garden, L.E., 2012. Application of LiDAR technology for measurement of time-varying free-surface profiles in a laboratory wave flume. *Coast Eng.* 68, 1–5. <https://doi.org/10.1016/j.coastaleng.2012.04.006>.
- Brodie, K.L., Slocum, R.K., McNinch, J.E., 2012. New insights into the physical drivers of wave runup from a continuously operating terrestrial laser scanner. *Oceans* 1–8. <https://doi.org/10.1109/OCEANS.2012.6404955>, 2012.
- Cete, C., 2019. Quantifying the Effect of Woody Vegetation on the Wave Loads on a Dike Using Remote Sensing. Large scale physical model tests [Delft University of Technology]. <http://resolver.tudelft.nl/uuid:88e2b629-efc9-48c8-b438-b250951200de>.
- De Rouck, J., Verhaeghe, H., Geeraerts, J., 2009. Crest level assessment of coastal structures — general overview. *Coast Eng.* 56 (2), 99–107. <https://doi.org/10.1016/j.coastaleng.2008.03.014>.
- De Vries, S., Hill, D.F., de Schipper, M.A., Stive, M.J.F., 2011. Remote sensing of surf zone waves using stereo imaging. *Coast Eng.* 58 (3), 239–250. <https://doi.org/10.1016/j.coastaleng.2010.10.004>.
- EurOtop, 2018. In: Van der Meer, J.W., Allsop, N.W.H., Bruce, T., De Rouck, J., Kortenhaus, A., Pullen, T., Schüttrumpf, H., Troch, P., Zanuttigh, B. (Eds.), *Manual on Wave Overtopping of Sea Defences and Related Structures. An Overtopping Manual Largely Based on European Research, but for Worldwide Application*. <http://www.overtopping-manual.com>.
- Guenther, G.C., Cunningham, A.G., LaRocque, P.E., Reid, D.J., 2000. Meeting the accuracy challenge in airborne bathymetry. Proceedings of EARSeL-SIG-Workshop LIDAR. https://earse.org/wp-content/uploads/2016/12/01_1_guenther1.pdf.
- Hanna, S.R., Heinold, D.W., 1985. *Development And Application of a Simple Method for Evaluating Air Quality Models* (Issue 4409). American Petroleum Institute.
- Hasselmann, K., Barnett, T.P., Bouws, E., Carlson, H., Cartwright, D.E., Enke, K., Ewing, J.A., Gienapp, H., Hasselmann, D.E., Kruseman, P., Meerburg, A., Mueller, P., Olbers, D.J., Richter, K., Sell, W., Walden, H., 1973. Measurements of wind-wave growth and swell decay during the joint north sea wave Project (JONSWAP). *Deutsches Hydrographisches Zeitschrift* 8 (12), 1–95. <http://resolver.tudelft.nl/uuid:f204e188-13b9-49d8-a6dc-4fb7c20562fc>.
- Hofland, B., Diamantidou, E., Van Steeg, P., Meys, P., 2015. Wave runup and wave overtopping measurements using a laser scanner. *Coast Eng.* 106, 20–29. <https://doi.org/10.1016/j.coastaleng.2015.09.003>.
- Holthuijsen, L.H., 2007. *Waves in Oceanic and Coastal Waters*. Cambridge University Press.
- Martins, K., Blenkinsopp, C.E., Zang, J., 2016. Monitoring individual wave characteristics in the inner surf with a 2-dimensional laser scanner (LiDAR). *J. Sens.* 1–11. <https://doi.org/10.1155/2016/7965431>, 2016.
- Maslov, D.V., Fadeev, V.V., Lyashenko, A.I., 2000. A shore-based lidar for coastal seawater monitoring. *Proc. EARSeL-SIG-Workshop LIDAR* 1, 46–52. <https://citeseerx.ist.psu.edu/viewdoc/download?doi=10.1.1.573.9310&rep=rep1&type=pdf>.
- Matias, A., Blenkinsopp, C.E., Masselink, G., 2014. Detailed investigation of overwash on a gravel barrier. *Mar. Geol.* 350, 27–38. <https://doi.org/10.1016/j.margeo.2014.01.009>.
- Mentaschi, L., Besio, G., Cassola, F., Mazzino, A., 2013. Problems in RMSE-based wave model validations. *Ocean Model.* 72, 53–58. <https://doi.org/10.1016/j.ocemod.2013.08.003>.
- Oosterlo, P., Hofland, B., Van der Meer, J.W., Overduin, M., Steendam, G.J., Nieuwenhuis, J.-W., Van Vledder, G.P., Steetzel, H., Reneerkens, M., 2019. Measuring (oblique) wave run-up and overtopping with laser scanners. *Proc. Coast. Struct.* 442–452. https://doi.org/10.18451/978-3-939230-64-9_045.
- Schüttrumpf, H.F.R., Van Gent, M.R.A., 2004. Wave overtopping at seadikes. *Proc. Coast. Struct.* 431–443. [https://doi.org/10.1061/40733\(147\)36](https://doi.org/10.1061/40733(147)36), 2003.
- Spore, N.J., Brodie, K.L., Swann, C., 2014. Automated Feature Extraction of Foredune Morphology from Terrestrial Lidar Data. American Geophysical Union. Fall Meeting 2014. <https://ui.adsabs.harvard.edu/abs/2014AGUFMEP31B3558S/abstract>.
- Steendam, G.J., Van der Meer, J.W., Van Hoven, A., Labrujere, A., 2017. Wave run-up simulations on real dikes. *Coast. Eng. Proc.* 1 (35), 42. <https://doi.org/10.9753/icce.v35.structures.42>.
- Streicher, M., Hofland, B., Lindenbergh, R.C., 2013. Laser ranging for monitoring water waves. In: The New Deltates Delta Flume. *ISPRS Annals Of Photogrammetry*, pp. 271–276. <https://doi.org/10.5194/isprannals-II-5-W2-271-2013>. Remote Sensing and Spatial Information Sciences, II-5/W2.
- Van der Meer, J.W., 2011. The Wave Run-Up Simulator. Idea, Necessity, Theoretical Background and Design. Van der Meer Consulting B.V. http://www.vandermeerconsulting.nl/downloads/stability_a/2011_wave_run_up_simulator.pdf.
- Van der Meer, J.W., Nieuwenhuis, J.-W., Steendam, G.J., Reneerkens, M., Steetzel, H., Van Vledder, G.P., 2019. Wave overtopping measurements at a real dike. *Proc. Coast. Struct.* 1107–1117. https://doi.org/10.18451/978-3-939230-64-9_111.
- Van der Meer, J.W., Schrijver, R., Hardeman, B., Van Hoven, A., Verheij, H., Steendam, G.J., 2010. Guidance on erosion resistance of inner slopes of dikes from three years of testing with the Wave Overtopping Simulator. *Coast. Mar. Struct. Breakw.: Adapt. Change* 2, 460–473. <https://doi.org/10.1680/cmsb.41318.0044>.
- Vosselman, G., Maas, H.-G., 2010. *Airborne and Terrestrial Laser Scanning*. Whittles Publishing.
- Vousdoukas, M.I., Kirupakaramoorthy, T., Oumeraci, H., De la Torre, M., Wübbold, F., Wagner, B., Schimmels, S., 2014. The role of combined laser scanning and video techniques in monitoring wave-by-wave swash zone processes. *Coast Eng.* 83, 150–165. <https://doi.org/10.1016/j.coastaleng.2013.10.013>.
- Wenneker, I., Spelt, B., Peters, H., De Ronde, J., 2016. Overview of 20 years of field measurements in the coastal zone and at the Petten sea dike in The Netherlands. *Coast Eng.* 109, 96–113. <https://doi.org/10.1016/j.coastaleng.2015.12.009>.
- Wübbold, F., Vousdoukas, M.I., Hentschel, M., Wagner, B., 2012. Towards autonomous coastal monitoring using 3D laser range scanners and camera vision. *Coast. Eng. Proc.* 1–6.
- Zijlema, M., Stelling, G., Smit, P.B., 2011. SWASH: an operational public domain code for simulating wave fields and rapidly varied flows in coastal waters. *Coast Eng.* 58 (10), 992–1012. <https://doi.org/10.1016/j.coastaleng.2011.05.015>.